Geomech. Geophys. Geo-energ. Geo-resour. (2022) 8:214
https://doi.org/10.1007/s40948-022-00504-0

ORIGINAL ARTICLE

Effect of pore pressure magnitude on the frictional properties and permeability evolution of fractures in schist

Ziyan Li · Derek Elsworth · Chaoyi Wang

Received: 22 February 2022 / Accepted: 9 September 2022 / Published online: 17 December 2022

Abstract Fluid injection-triggered seismicity has increased dramatically over the last decade with elevated pore fluid pressures acting as a prime culprit. Thus, understanding the effect of pore fluid pressure on the mechanical and hydrologic behavior of fractures and faults will illuminate the contributing and dominant physical processes. We present concurrent measurements of shear displacement and flow to quantify the evolution of frictional strength, stability and permeability of schist during the full seismic cycle. We use a miniature double direct shear (mini-DDS) apparatus to conduct velocity stepping (VS for stability) and slide-hold-slide (SHS for frictional healing). Our results demonstrate that increasing pore fluid pressures can stabilize frictional slip under otherwise invariant effective stresses. This implies that elevated pressures favor stable slip as a material characteristic even in the absence of decreasing critical fault stiffness (thereby increasing stability) as a result of decreased effective stress. However, the magnitude of pore pressure does not control permeability evolution during velocity steps as pore pressure does not control aperture dilation/compaction for an invariant effective normal stress. During SHS tests, it is shown that the magnitude of normalized permeability change increases with hold time and that the rate of permeability change generally decreases with the increment of pore fluid pressure, suggesting that high fluid pressures may limit permeability change during interseismic response, although creep response may still dominate over the long term.

Article Highlights

- Increasing pore fluid pressures stabilizes frictional slip under invariant effective stresses.
- The magnitude of pore pressure is not a dominant control on permeability evolution for an invariant effective normal stress.
- Elevated pore fluid pressure reduces healing rate and limits permeability change rate for invariant effective normal stresses.

Keywords Rock mechanics experiments · Permeability evolution · Frictional behavior of fractures · Fluid pressurization

Z. Li (✉) · D. Elsworth · C. Wang (✉)
Department of Energy and Mineral Engineering, The Pennsylvania State University, University Park, PA, USA
e-mail: ziyan.li1@ucalgary.ca

C. Wang
e-mail: chaoyi.wang1@ucalgary.ca

Z. Li · D. Elsworth · C. Wang
G3 Center and EMS Energy Institute, The Pennsylvania State University, University Park, PA, USA

D. Elsworth
Department of Geosciences, The Pennsylvania State University, University Park, PA, USA

1 Introduction

Elevated pore pressures are frequently observed with triggered seismicity in both natural (Hubbert and Rubey 1959; Sibson 1973; Andrews 2002) and engineered geological systems that include wastewater injection, hydraulic fracturing, CO_2 sequestration, and geothermal operations (Deichmann and Giardini 2009; Frohlich and Brunt 2013; Bao and Eaton 2016; Deng et al. 2016; Yoon et al. 2017;). The high pressurized fluid that injected into the reservoir may activate pre-existing nearby faults once the shear stress along the fault reaches a critical value τ_c. Based on the concept of effective stress combined with a Coulomb failure criterion, for a given fault, the critical shear stress, $\tau_c = \mu\,(\sigma_N - P_f)$, is the product of a friction coefficient μ (ranging from 0.6 to 0.85 in most crustal rock types (Byerlee 1968) and the effective normal stress, $\sigma_N^{'} = \sigma_N - P_f$, applied on the fault. Thus, the higher pore pressure P_f decreases the effective normal stress and therefore lead to fault slip.

The onset of fault slip may be seismic or aseismic depending on the frictional behavior of the fractures (Dieterich and Kilgore 1996; Marone 1998a, b). In addition, fracture permeability may evolve in either of these stability modes. Experimental observations have demonstrated that the friction-stability-permeability relationship of a fracture is significantly controlled by mineral composition (Fang et al. 2018) in addition to roughness and other parameters. The different modes of slip modify asperity contact distribution and determine the permeability changes (Ishibashi et al. 2018). Additionally, changes in driving velocity, manifest as a change in shear rate, also result in fracture dilation/compaction with such aperture change directly controlling permeability evolution (Faoro et al. 2009; Zhang et al. 1999).

Prior research have studied the impact of fluid pressure on stability of fault /fractures with conflicting results. Elevated pore pressure may lead to fault slip due to reduced effective normal stress and may lead to the transition from stable to unstable slip (Sawai et al. 2016; Ougier-Simonin and Zhu 2015; Scuderi et al. 2017). Conversely, some experimental studies have shown that the increasing fluid pressure increases friction at the same effective stress, which stabilizes the fault. (den Hartog and Spiers 2013; French and Zhu 2017; Xing et al. 2019). These apparent disagreements may result from differing mineral compositions of the samples or the influence of other first-order controls. However, the isolated impact of pore pressure alone on stability parameters has yet to be distinguished from the effect of effective stresses alone.

In the following, we explore the impact of pore pressure on frictional behavior of schist fractures, including friction coefficient, stability parameters, characteristic displacement and frictional healing rate. We conduct a series of velocity-stepping and slide-hold-slide experiments with varying pore pressures, specifically to isolate the impact of pore pressure on the frictional properties of fractures. We increase confining pressures lockstep with pore fluid pressures to retain effective stresses constant. Additionally, we examine the corresponding permeability response throughout the experiments. Our results provide a fundamental understanding of hydro-mechanical coupling processes for earthquakes induced by fluid injection, and for the nucleation of seismicity. This can be applied to predict fluid migration by industrial injection activities in the reservoir.

2 Experimental method

We evaluate the influence of pore pressure on the frictional properties of faults/fractures—including frictional strength and stability and frictional healing rate together with the concurrent measurement of fracture permeability—to understand the coupled mechanical-hydrological behavior of faults/fractures. We explore this response through coupled shear-flow experiments on fractures of schist (EGS-Collab Experiment) using a novel mini DDS apparatus (Fig. 1a). The samples are collected from the Precambrian Poorman formation at the Sanford Underground Research Facility (SURF), located at the former Homestake Gold Mine, Lead, South Dakota (White et al. 2018). The most abundant rocks of the Poorman Schist formation are the fine-grained carbonaceous banded mica (muscovite) schists and slates (Ye et al. 2019). To create the double-direct-shear geometry, the sample is configured as a prismatic rock coupon sandwiched between two half-cylindrical cores within a hydraulically isolating latex jacket. Sample dimensions and geometry are shown in Fig. 1b. This experimental configuration enables accurate measurement of friction by minimizing the impact of jacket/membrane restraint. We

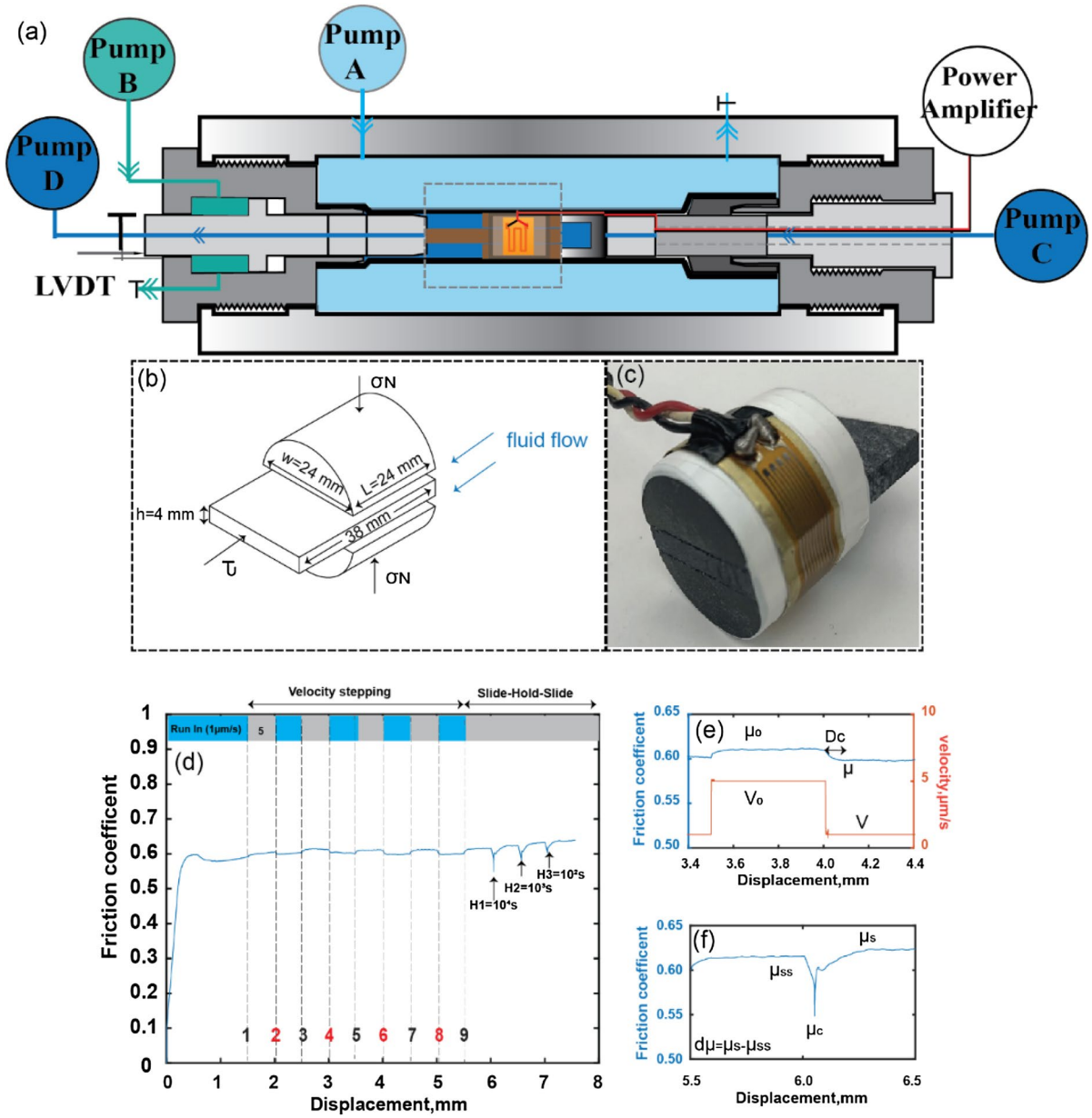

Fig. 1 **a** Experimental configuration. **b** sample geometry and dimensions. **c** Sample core with strain gauge and belt. **d** A typical curve showing frictional strength versus shear displacement during velocity-stepping (VS) and slide-hold-slide (SHS) experiments. **e** Responses in the frictional coefficient caused by shear velocity up-steps and down-steps in VS experiments. **f** Response of frictional healing in SHS experiments

first flatten the contacting rock using wet abrasion to achieve consistent flatness. 1200 grit aluminum oxide powder was then used to ground the contacting surface to create reproducible roughness. The entire assembled sample is then installed in a pressurized core holder, where shear stress normal stress, and pore pressure are individually controlled by servo-controlled precision hydraulic pumps (A, B; Fig. 1a). Shear displacement is measured by a linear variable differential transducer (LVDT) that attached to the loading piston driven by Pump B. Flow rate is created by the pressure difference ($\Delta p \approx 10$ Kpa) between

Table 1 Summary of experiments

Exp No.	Confining pressure KPa	Pup KPa	Pdn KPa	Effective stress Kpa	μ_p	μ_{ss}
1	3200	200	190	3000	0.569	0.564
2	3400	400	390	3000	0.572	0.570
3	3600	600	590	3000	0.582	0.577
4	3800	800	790	3000	0.598	0.579
5	4000	1000	990	3000	0.625	0.619

upstream (Pump C) and downstream (Pump D) reservoir, with pressures controlled by hydraulic pumps. Permeability is then calculated based on Darcy's Law assuming steady state flow as,

$$k = \frac{\mu_w l}{A}\frac{(q + whv)}{\Delta p} \tag{1}$$

where μ_w is the fluid viscosity (8.9×10^{-4} Pa·s), l is the flow path length, w and h, are width and height of the central prism respectively, A is the cross-sectional area of the sample perpendicular to the flow path, q is the flow rate though the fracture, v represents the slip velocity. The term whv is used to correct the center block intrusion into the specimen REV. Hydraulic aperture (b_h) is estimated via the cubic law (Witherspoon et al. 1980), adapting the DDS configuration that is designed to our system (Eq. 4, Im et al. 2019) as,

$$b_h = \left(\frac{(Q + whv)}{2}\frac{l}{\Delta P}\frac{12\mu_w}{w}\right)^{1/3}. \tag{2}$$

An alternative method to estimate the change in mechanical aperture is to record circumferential strain (ε) of the sample assembly and then convert this to fracture normal displacement by multiplying this by half of the strain belt length (L_s) (Im et al., 2019). The circumferential strain is measured by a strain gauge attached to the stain belt, which consists of a 0.127 mm thick aluminum shim wrapped around the sample covering the two fractures (Fig. 1c). Thus, aperture change is defined as,

$$b_s = \varepsilon * \frac{1}{2}L_s. \tag{3}$$

We conduct all experiments under identical normal effective stresses of 3 MPa, including pressure saturation of the sample until flow stabilizes. Differential pore pressure (Pup-Pdn) is held constant (10 kPa) and elevated slowly to new incremented value (see Table 1). Confining stress increases concomitantly with pore fluid pressure (Pc) so that the effective normal stress is maintained constant. The sample is subsequently sheared at constant rate (1 μm/s) until stabilized. We then define the peak friction coefficient (μp), steady state friction coefficient (μss), and calculate initial steady-state fracture aperture (bh0).

We conduct velocity-stepping (VS) and slide-hold-slide (SHS) experiments with typical procedures and responses shown in Fig. 1d. VS tests are conducted to get rate-and-state parameters by changing shear velocity between 1 (blue) and 5 μm/s (grey) step-by-step. The step number labelled in Fig. 1d shows the velocity increasing step in black, and velocity decreasing step in red. Detailed step information is listed in Table.1. Following each velocity step, we allow a shear displacement of 0.5 mm to achieve a new steady state for consistent measurement frictional parameters. We observe that a velocity increasing step produces an instantaneous increase in the frictional strength that decays over a critical slip distance, D_c (Dieterich 1979, 1981). Our measurements confirm this behavior. We calculate frictional stability by calculating the rate and state parameter (a–b):

$$\mathbf{a-b} = \frac{\mu - \mu_0}{\ln\left(\frac{v}{v_0}\right)} \tag{4}$$

where μ_0 and μ are the steady state friction at sliding velocities of v_0 and v. The stability factor (a–b) and characteristic displacement ($\mathbf{D}_c$) are obtained from the measurement as illustrated in Fig. 1e. We conduct SHS tests involving three distinct hold periods, representing different times of interseismic repose, of 10^4, 10^3 and 10^2 s respectively. During the slide-hold-slide sequence, $\Delta\mu$ is calculated by the relative static friction change as illustrated in Fig. 1f.

Table 2 Stepping sequence for velocity stepping (VS) experiments

Step No	1	2	3	4	5	6	7	8	9
velocity step(μm/s)	1–5 (+)	5–1 (−)	1–5 (+)	5–1 (−)	1–5 (+)	5–1 (−)	1–5 (+)	5–1 (−)	1–5 (+)
Axial displacement(μm)	~1500	~2000	~2500	~3000	~3500	~4000	~4500	~5000	~5500

3 Results

We present the results for (1) frictional properties of the schist including the stability factor (a–b) and characteristic displacement (D_c) during VS experiments and healing rate (β) during SHS experiments, and (2) permeability response to stability in VS tests, and (3) permeability evolution during the interseismic period in the SHS experiments.

3.1 Frictional properties

We observe that frictional strength from all experiments exhibits a peak frictional strength (μ_p) from ~0.57 to 0.63 decaying to a residual steady state (μ_{ss}) strength of ~0.56 to 0.62 at shear displacement of 1 mm (Table 2). The peak strength and steady sate friction coefficient shows a linear positive trend with pore pressure magnitude.

Figure 2 shows frictional properties under varying pore fluid pressure. Colors from cold to warm, as shown in Fig. 2a, represents fluid pressures from 0.2 to 1 MPa. Open upward-triangles represent velocity increasing steps and solid downward-triangles velocity decreasing step. We show the magnitude of the frictional stability parameter (a–b) corresponding with velocity steps under each pore fluid pressure in Fig. 2a. The positive (a–b) values show that schist has velocity strengthening behavior. An oscillating response of frictional stability (a–b) for both velocity-increasing and -decreasing steps are observed, with a gradually weakening as pore pressure increase. We plot stability parameter for both velocity increasing and decreasing steps against each pore pressure. The average value of (a–b) with the 99% confidence interval is reported in Fig. 2b. The average (a–b) values (solid circles) increase with an elevation in the pore fluid pressure, indicating that increased pore fluid pressure has a stabilizing effect on slip. We show the change in characteristic displacement (D_c) relative to the velocity step number-sequence for each pore pressure in Fig. 2c. The decreasing trend of D_c with successive velocity step indicates that a shorter displacement is needed to reach steady state. This may result from the changes in shear fabric and shear localization. An increase in average D_c ranges from ~70 to 100 μm as pore fluid pressure increases (Fig. 2d). This implies that the elevated pore pressure could produce longer characteristic displacement, and result in lower critical fault rheologic stiffness, and thus strengthen the fault.

Figure 2e shows healing results for experiments conducted at each pore fluid pressure. Frictional healing (dμ) increases linearly with the logarithm of hold time, consistent with previous work (Marone, 1998a, b; Yasuhara et al., 2005; Carpenter et al., 2016). We display the healing rate ($\beta = \Delta\mu/\log 10 t_h$, where t_h is hold time) at each pore fluid pressure in Fig. 2f. The rate of healing decreases with increasing pore fluid pressure, implying that high pore fluid pressure inhibits healing.

3.2 Permeability responses to frictional stability

We present a typical curve of dynamic permeability (black) during run-in and VS tests in Fig. 3a. Permeability is converted to hydraulic aperture (red) using Eq. (2) and compared with the strain gage measured aperture (blue) in the same plot. The overlap of these two aperture evolution curves indicates the agreement of the two methods for estimating aperture normal displacement. Permeability reduces within a millimeter of initial slip, potentially representing shear-driven comminution of fracture asperities. This permeability response is consistent with previous studies (e.g., Fang et al. 2017; Im et al. 2018; Ishibashi et al. 2016). During the VS test, the permeability evolution exhibits rate-and-state behavior. An enhancement in permeability occurs when velocity decreases, followed by a constant residual permeability that is higher than the previous step. Conversely, permeability reduces as velocity increases. This characteristic response is amplified with increasing shear displacement. A similar trend is also observed in aperture change. To

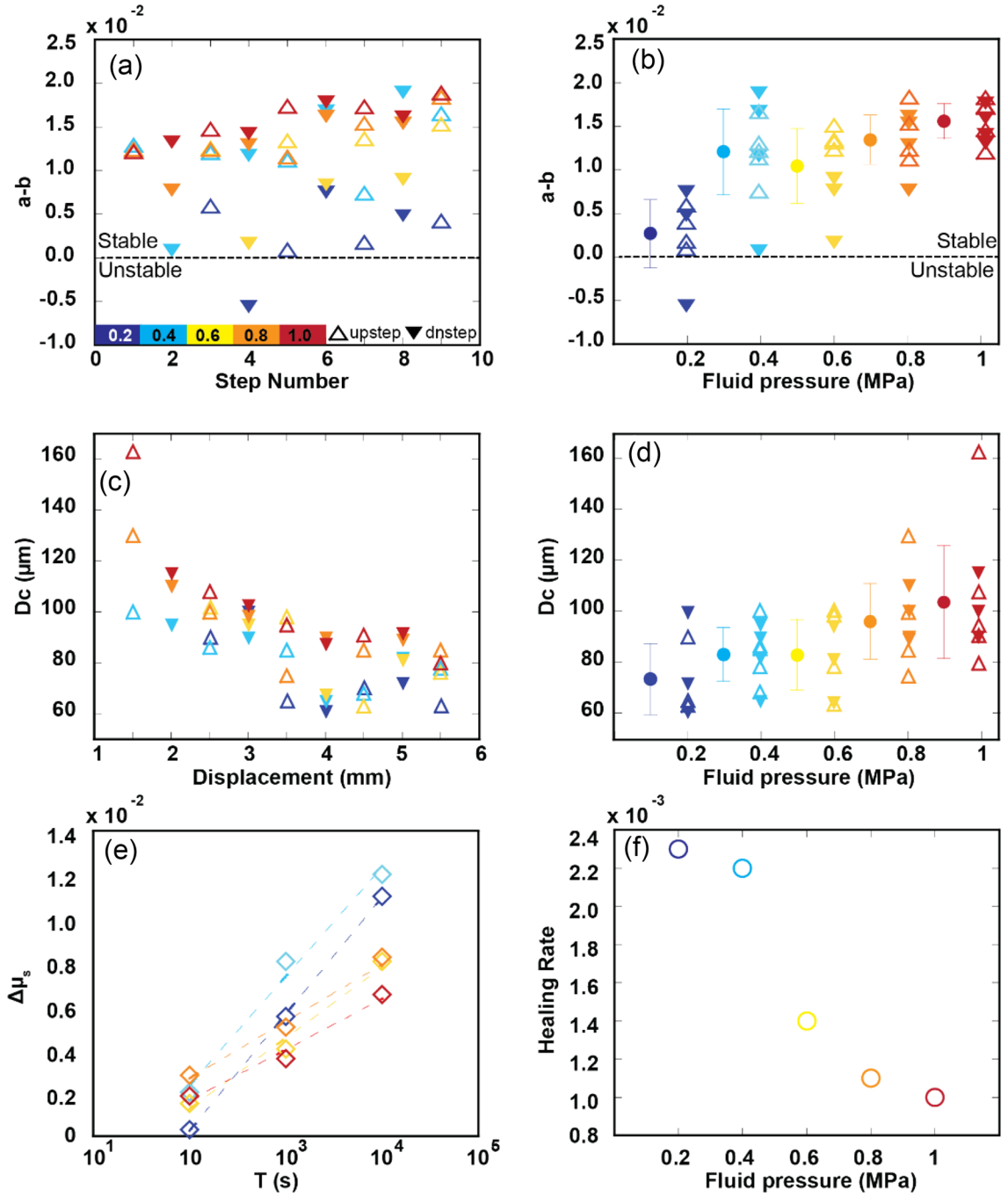

Fig. 2 Frictional properties of schist under varying pore pressure. **a** Stability parameter (*a*-*b*) corresponding to velocity steps under different pore pressures. **b** (*a*-*b*) values for both velocity-increasing (open symbols) and -decreasing (closed symbols) steps under different pore pressures and average (*a*-*b*) values with 90% confidence interval are shown to the left of symbols. **c** Characteristic displacement (D_c) responses to velocity steps under different pore pressures. **d** D_c values for both velocity-increasing and -decreasing steps, with average values of D_c of all velocity steps together with their 90% confidence intervals. **e** Frictional healing increment as a function of logarithm of hold time. **f** Frictional healing rate under different pore fluid pressures

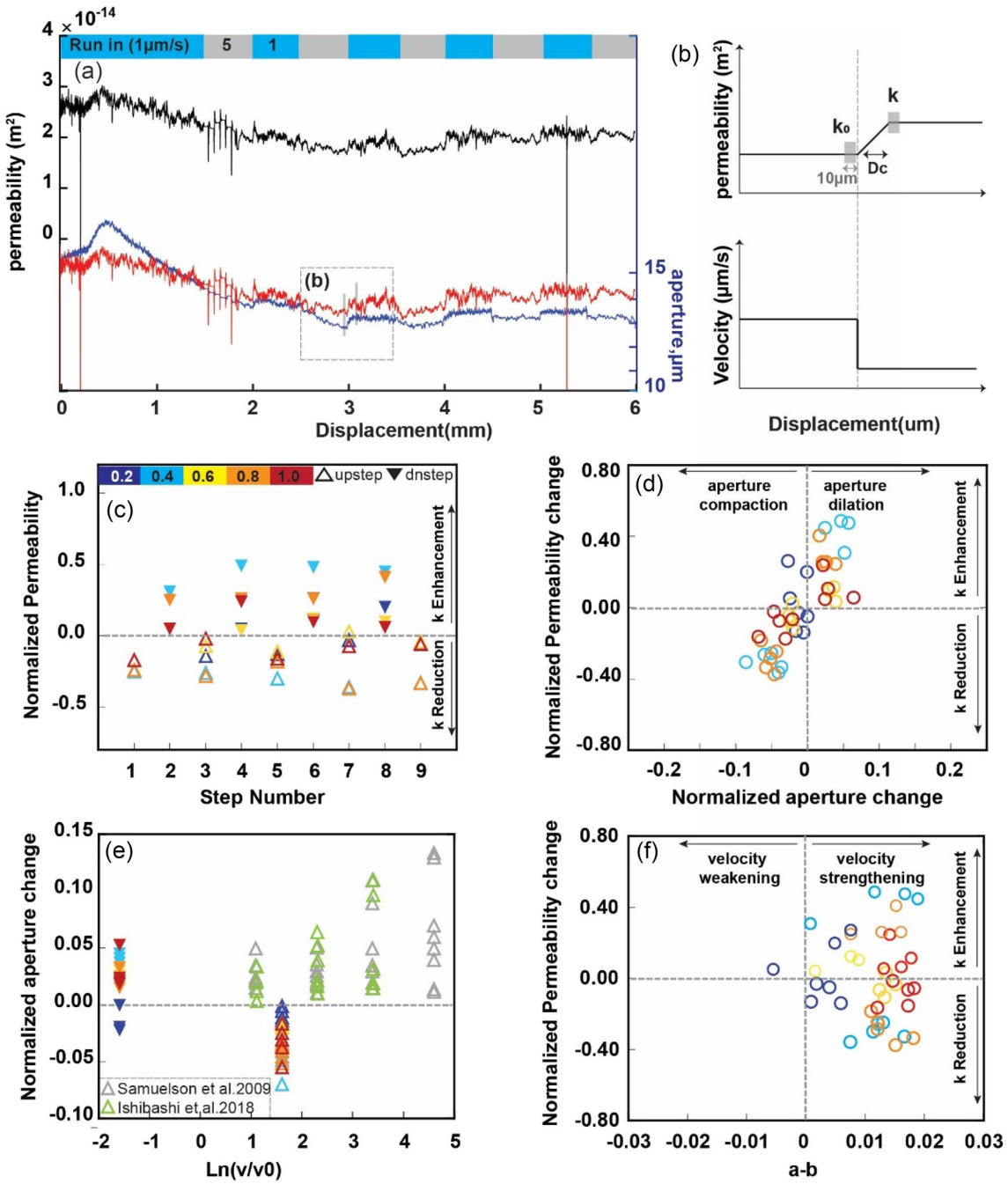

Fig. 3 **a** Permeability evolution during run-in and VS testing. **b** Representative normalized permeability changes due to shear velocity steps. **c** Normalized permeability change for successive velocity steps for various pore fluid pressures. **d** Normalized permeability versus normalized aperture change. **e** Normalized aperture change with magnitude of velocity upstep (open symbols) or downstep (filled symbols). **f** Normailized permeability change versus the stabilty parameter (*a–b*)

estimate the fracture permeability change resulting from velocity steps, we define normalized permeability change as

$$\frac{\Delta \mathbf{k}}{\mathbf{k}_0} = \frac{\mathbf{k} - \mathbf{k}_0}{\mathbf{k}_0} \tag{5}$$

where permeability change ($\Delta\mathbf{k}$) is the difference of the permeability before ($\mathbf{k}_0$) then after ($\mathbf{k}$) shear velocity step. To minimize the impacts of permeability fluctuation, both $\mathbf{k}_0$ and k are calculated by the average fracture permeability over a shear-displacement window ± 10 μm as shown in upper part of Fig. 3b. A negative normalized permeability change represents permeability reduction due to shear velocity change, and a positive normalized permeability change the converse. The same method is applied to calculate normalized strain-gage-measured aperture change ($\Delta b/b_0$). Normalized permeability change relative to velocity step number-sequence is shown for all experiments conducted at different pore fluid pressures (Fig. 3c) and shows that permeability reduces as velocity increases and enhances as velocity decreases. At the same effective stress, permeability changes result mainly from compaction/dilation of fractures due to the velocity change. This is suggested by the linear positive relation between normalized permeability change with change in aperture, as shown in Fig. 3d. Most of the data inhabit the first and third quadrants, indicating that dilation results in permeability enhancement and compaction leads to permeability reduction—as logically expected, absent the presence of wear products. A few outliers inhabit the second quadrant, suggesting that during the aperture closure, permeability is increasing. This may result from particle mobilization and unclogging effects due to the mobilization of wear products by fluid flow (e.g. Figure 9 in Candela et al. 2015).

The normalized aperture change under varing fluid pressure versus velocity step size (ln(v/v0)) is shown in Fig. 3e. Normalized changes in aperture are positive (range 1–%) for velocity downsteps (inverted solid triangles) except for a negative outliers (0 ~ 3%) when pore pressure is as low as 0.2 MPa. Conversly, the normalized aperture change, ranging from 0 to 7%, are all negative for velocity upsteps. These trends suggest that fractures dilate when shear velocity decreases and compact when shear velocity increases. This is counter to previous observations both in gouge and on fractures, as shown by the open green and grey triangles (Samuelson et al. 2009; Ishibashi et al. 2018). A mechanism explaining this apparent contradiction is advanced later. Considering the systematics of permeability enhancement with aperture dilation, all data appear exlusively in the first and forth quadrants in Fig. 3f, indicating a correlation in permeability enhancement with dilation—as anticipated. Both pemeability enhancement (first quadrant) and reduction (forth quadrant) can occur during velocity stepping. This suggests that pore pressure may not be a dominating factor in controlling aperture dilation/compaction based on velocity change at the same effective normal stress.

3.3 Permeability evolution during interseismic repose

The evolution of permeability is shown with both displacement (Fig. 4a) and hold time (Fig. 2b) during shear-hold-slide (SHS) experiments. Shear slip (blue) and intervening holds (grey) are denoted by the top bar. In these SHS experiments, samples are sheared at a prescribed load point velocity (5 μm/s) followed by 'holds' initiated by setting the load point velocity to zero. Detailed permeability evolution within a single representative SHS experiment for the dashed-boxed inset in Fig. 4b is highlighted and zoomed-in in Fig. 4c. At the onset of a hold, we detect a permeability enhancement after sliding ceases but before creep initiates. Permeability increases to a maximum value before returning to its initial level. During hold periods, permeability continuously declines without any evidence of stabilization. Upon reloading and reinitiating the slide, permeability decreases significantly until reaching a steady state. Normalized permeability changes during a hold (Fig. 4c) where the initial (k_0) and end permeability (k_1) in the second hold (H2) are marked by light bule with the permeability value shown alongside. We calculate the average value of permeability within a 20 s window at the initiation and termination of each hold when permeability stabilizes.

Normalized permeability change during holds is shown relative to the log of hold time is shown in Fig. 4d. The magnitude of normalized permeability change increases with hold time. We then define permeability change rate as the slope of the normalized permeability change versus hold time and relative to fluid pressure. Permeability change rate generally decreases with an increment of pore fluid pressure (Fig. 4e), suggesting that high fluid pressure may resists permeability change during the interseismic response. A peak in the rate of change of permeability is observed at fluid pressure of 0.4 MPa (Fig. 4e). This may result from sample bias from the other

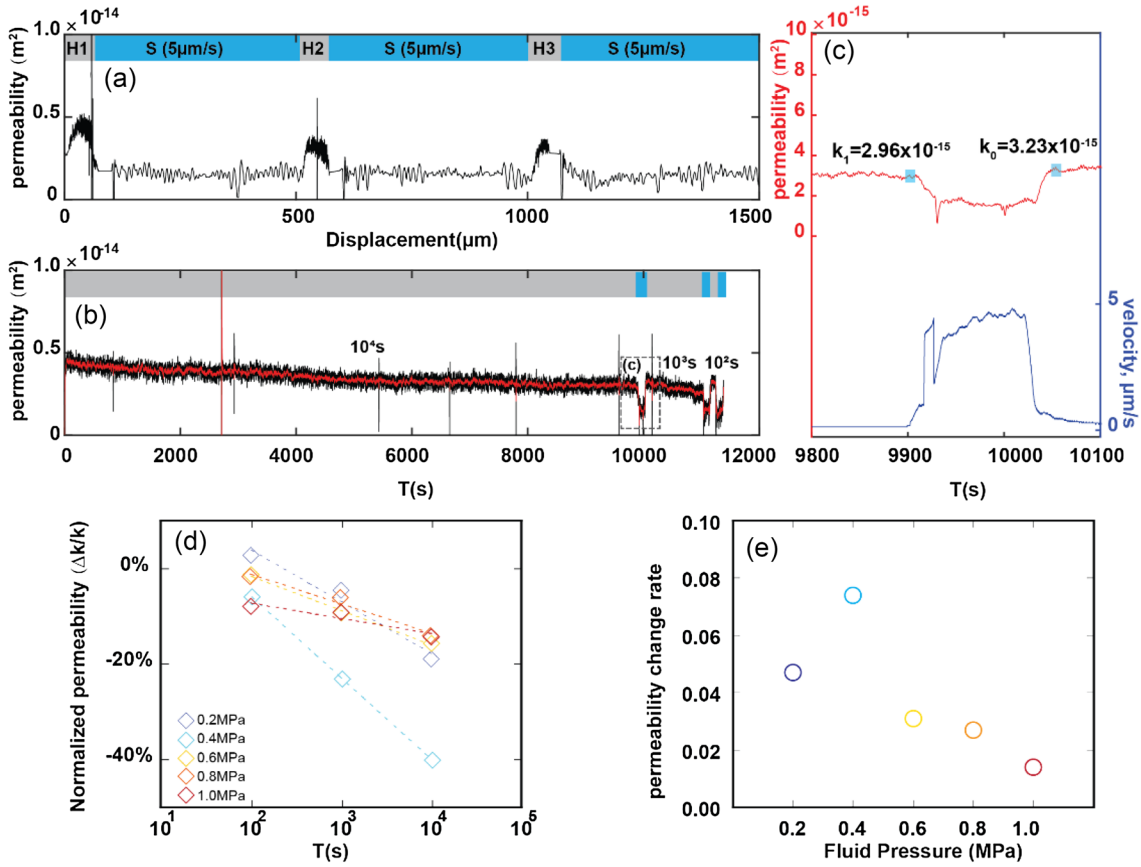

Fig. 4 **a** Permeability evolution versus displacement and with **b** time during slide-hold-slide experiments. **c** Permeability evolution during holds, where normalized permeability change is defined. **d** Normalized permeability versus hold time under varying pore fluid pressures. **e** Permeability change rate versus fluid pressure

experiments, which is acceptable. Even if we cut the sample from the same core and then prepare the sample to create reproducible roughness, there remains the possibility that the sample roughness for Experiment No.2 (fluid pressure is 0.4 MPa) is slightly lower than the others, manifest as a lower normalized permeability (Fig. 4d) and higher permeability change rate during the SHS tests (Fig. 4e).

4 Discussion

4.1 Impact of elevated pore pressure on frictional behavior

At the same effective pressure, our results prove that the elevated pore pressures leads to an increase in (a–b) that stabilizes fault slip. Several works have shown the same effect of pore fluid pressure on granite (Brace and Martin1968; Martin 1980), serpentinite (French and Zhu 2017), antigorite, olivine, quartz, and chrysotile (Xing et al 2019), suggesting that the resulting stabilizing effect may not be sensitive to lithology. The stabilizing effect comes from dilatant hardening, where cracks grow during brittle deformation, resulting in larger pore space and reduced pore pressure where fluid transport is undrained. This results in a drop in the local effective stress and a staunching of cracks growth or frictional slip (Rice 1975; Rudnicki and Chen 1988; Xing et al. 2019). It shows that a larger D_c results in a lower critical stiffness that favor stable slip. This implies that slip for the schist examined here will favor stable slip under room temperature conditions. This study show that elevated pore pressures result in increment in apparent slip velocity dependence. This study highlights

the importance of considering fluid pressure when estimating the slip behavior of fault. Other minerals may also show a correlation between apparent velocity rate dependence and fluid pressure—although this remain to be investigated.

4.2 Permeability response to stepped shear velocities

Previous work has noted that fracture apertures/fault gouges characteristically dilate during shearing and that the magnitude of this dilation increases with increasing velocity step size (Samuelson et al. 2009; Ishibashi et al. 2018; Li et al. 2019). This is because the grains of the compacted asperities/dense granular material interlock during compaction and are constrained from moving. When sheared, relative motion between neighboring asperities/grains produces a bulk expansion of the fracture aperture/fault gouge—manifest as dilation. Our experiments show a contrasting result, where aperture compaction is observed when fractures are subjected to shear deformation with an increase in shear velocity. This is because the wear products generated during shearing are in a relatively loose state under low effective normal stress, and therefore have the freedom to move relative to each other. Since the schist exhibits velocity strengthening behavior, a higher corresponding shear stress results when shear velocity is suddenly increased. Additionally, there can be little dilatant hardening in our experiments as pore space is refilled with water as soon as it is created, indicating that shear stress mainly acts on comminuting mineral particles generated from early breakage of asperities. This will result in the continuous compaction of wear products, rather than their dilation. Under our experimental conditions, dilation may occur as shear rate increases when the hard minerals (such as quartz) produced by shear are difficult to comminute. These may then be translated and rotated during the shearing process (Fang et al. 2016). However, this is not a dominating factor to control fracture permeability, especially when the roughness of the surface is low, and large granular particles cannot be generated as only small asperities break. Considering all these factors, it is reasonable that shear at a higher rate results in compaction, and a lower shear velocity results in dilation under our experimental condition. As fracture dilatancy of the aperture has a controlling effect on permeability, normalized permeability change has a positive linear relationship with fracture aperture changes due to velocity change—excepting some outliers when compaction results in permeability enhancement due to particle mobilization and unclogging driven by fluid flow (Fig. 3d). This explains why permeability enhances for velocity down-steps steps and reduces for velocity up-steps. If these results can be applied to real faults, we would conclude that dilation would be largely independent of fluid pressure in a fault zone under the same effective stress, and faults tend to seal itself once it is reactivated and shear with higher velocity (Fang et al. 2017; Faoro et al. 2009; Wang and Scholz 1994).

5 Conclusions

We perform laboratory experiments to systematically explore the controls of pore pressure on the frictional behavior and healing on schist fractures. We conclude the following:

Our results show that the average frictional stability parameter and characteristic displacement both increase with an elevated pore pressure. This suggests that increased pore pressure leads to an increase in the apparent slip velocity dependence of frictional sliding, and thus has a stabilizing effect on slip. Higher pore pressure also increases characteristic displacement, resulting in a lower critical fault rheologic stiffness and hence in the strengthening of faults.

The result shows that most of normalized permeability changes linearly with normalized aperture change, indicating that aperture compaction/dilation is the key mechanism to determine fracture permeability. However, increasing pore pressure does not always cause increment in permeability under the same effective stress. This may suggest that pore pressure is not a dominant factor in controlling aperture dilation/compaction based on velocity stepping at the same effective normal stress. Therefore, changes in the magnitude of pore pressure do not dominantly control permeability evolution during a stepped velocity change.

Acknowledgements This work is a partial result of support from the DOE EGS Collab Project: Stimulation Investigations for Geothermal Modeling, Analysis and Validation and from DOE award DE-EE0008763. This support is gratefully acknowledged. EGS-Collab Team—Author list appended at the end of the manuscript.

EGS-Collab Team members by organization DOE: L. Boyd, Z. Frone, E. Metcalfe, A. Nieto, S. Porse, W. Vandermeer. INL. R. Podgorney, G. Neupane. LBNL: J. Ajo-Franklin, P.J. Cook, P.F. Dobson, C.A. Doughty, Y. Guglielmi, M. Hu, R.S. Jayne, K. Kim, T. Kneafsey, S. Nakagawa, G. Newman, P. Petrov, M. Robertson, J. Rutqvist, M. Schoenball, E.L. Sonnenthal, F.A. Soom, C. Ulrich, C.A. Valladao, T. Wood, Y.Q. Zhang, Q. Zhou. LANL: L. Huang, Y. Chen, B. Chi, Z. Feng, L.P. Frash, K. Gao, E. Jafarov, S. Karra, N. Makedonska, W. Pan, R. Pawar, N. Welch. LLNL: P. Fu, R.J. Mellors, J.P. Morris, M.M. Smith, D. Templeton, H. Wu. NETL: J. Moore, S. Brown, D. Crandall, P. Mackey, T. Paronish, S. Workman. NREL: B. Johnston, K. Beckers, J. Weers. ORNL: Y. Polsky, Monica Maceira, Chengping Chai. PNNL: A. Bonneville, J.A. Burghardt, J. Horner, T.C. Johnson, H. Knox, J. Knox, B.Q. Roberts, P. Sprinkle, C.E. Strickland, J.N. Thomle, V.R. Vermeul, M.D. White. SNL: D. Blankenship, M. Ingraham, J. Pope, P. Schwering, A. Foris, DK King, J. Feldman, M. Lee, J. Su. SURF: T. Baumgartner, J. Heise, M. Horn, B. Pietzyk, D. Rynders, G. Vandine, D. Vardiman, Subs: Thomas Doe, TDoeGeo Rock Fracture Consulting; Golder Associates Inc; J. McLennan, University of Utah. CSM – Y.S. Wu, J. Miskimins, P. Winterfeld, K. Kutun. Stanford—M.D. Zoback—A. Singh, Stanford—R.N. Horne, K. Li, A. Hawkins, Y. Zhang. Mattson Hydrology LLC: E. Mattson. Penn State—D. Elsworth, K.J. Im, Z. Li, C.J. Marone, E.C. Yildirim. Rice University—Jonathan Ajo-Franklin. The University of Oklahoma—A. Ghassemi, Dharmendra Kumar, Varahanaresh Sesetty, Alex Vachaparampil. University of Wisconsin -Madison– H.F. Wang, Hiroki Sone, Kate Condon, and Bezalel Haimson. South Dakota School of Mines and Technology—W. Roggenthen, C. Medler, N. Uzunlar, Carson Reimers. ResFrac—M.W. McClure

Declarations

Conflict of interest On behalf of all authors, the corresponding author states that there is no conflict of interest.

References

Andrews DJ (2002) A fault constitutive relation accounting for thermal pressurization of pore fluid. J Geophys Res: Solid Earth 107(B12):ESE-15

Bao X, Eaton DW (2016) Fault activation by hydraulic fracturing in western Canada. Science 354(6318):1406–1409

Brace WF, Martin RJ (1968) A test of the law of effective stress for crystalline rocks of low porosity. Int J Rock Mech Mining Sci Geomech Abstr 5(5):415–426

Byerlee JD (1968) Brittle-ductile transition in rocks. J Geophys Res 73(14):4741–4750

Candela T et al (2015) Flow rate dictates permeability enhancement during fluid pressure oscillations in laboratory experiments. J Geophys Res: Solid Earth 120(4):2037–2055

Carpenter BM, Matt JI, Marone C (2016) Laboratory observations of time-dependent frictional strengthening and stress relaxation in natural and synthetic fault gouges. J Geophys Res: Solid Earth 121(2):1183–1201

Deichmann N, Giardini D (2009) Earthquakes induced by the stimulation of an enhanced geothermal system below Basel (Switzerland). Seismol Res Lett 80(5):784–798

den Hartog SA, Spiers CJ (2013) Influence of subduction zone conditions and gouge composition on frictional slip stability of megathrust faults. Tectonophysics 600:75–90

Deng K, Liu Y, Harrington RM (2016) Poroelastic stress triggering of the December 2013 Crooked Lake, Alberta, induced seismicity sequence. Geophys Res Lett 43(16):8482–8491

Dieterich JH (1979) Modeling of rock friction: 1. Experimental results and constitutive equations. J Geophys Res: Solid Earth 84(B5):2161–2168

Dieterich JH (1981) Constitutive properties of faults with simulated gouge. Mech Behav Crustal Rocks 24:103–120

Dieterich JH, Kilgore BD (1996) Imaging surface contacts: power law contact distributions and contact stresses in quartz, calcite, glass and acrylic plastic. Tectonophysics 256(1–4):219–239

Fang Y, Wang C, Elsworth D, Ishibashi T (2016) Friction-permeability relationships for reservoir caprocks. Paper presented at the 50th U.S. Rock Mechanics/Geomechanics Symposium, Houston, Texas

Fang Y et al (2017) Frictional stability-permeability relationships for fractures in shales. J Geophys Res: Solid Earth 122(3):1760–1776

Fang Y et al (2018) Permeability evolution and frictional stability of fabricated fractures with specified roughness. J Geophys Res: Solid Earth 123(11):9355–9375

Faoro I et al (2009) Influence of shear and deviatoric stress on the evolution of permeability in fractured rock. J Geophys Res: Solid Earth. https://doi.org/10.1029/2007JB005372

French ME, Zhu W (2017) Slow fault propagation in serpentinite under conditions of high pore fluid pressure. Earth Planet Sci Lett 473:131–140

Frohlich C, Brunt M (2013) Two-year survey of earthquakes and injection/production wells in the Eagle Ford Shale, Texas, prior to the Mw4. 8 20 October 2011 earthquake. Earth Planet Sci Lett 379:56–63

Hubbert MK, Rubey WW (1959) Role of fluid pressure in mechanics of overthrust faulting: I. Mechanics of fluid-filled porous solids and its application to overthrust faulting. GSA Bull 70(2):115–166

Im K, Elsworth D, Fang Yi (2018) The influence of preslip sealing on the permeability evolution of fractures and faults. Geophys Res Lett 45(1):166–175

Im K, Elsworth D, Wang C (2019) Cyclic permeability evolution during repose then reactivation of fractures and faults. J Geophys Res: Solid Earth 124(5):4492–4506

Ishibashi T et al (2016) Linking microearthquakes to fracture permeability change: the role of surface roughness. Geophys Res Lett 43(14):7486–7493

Ishibashi T et al (2018) Friction-stability-permeability evolution of a fracture in granite. Water Resour Res 54(12):9901–9918

Li Z et al (2019) A new apparatus for the concurrent measurement of friction and permeability evolution in fault gouge. Int J Rock Mech Mining Sci 121:104046

Marone C (1998a) Laboratory-derived friction laws and their application to seismic faulting. Annu Rev Earth Planet Sci 26(1):643–696

Marone C (1998b) The effect of loading rate on static friction and the rate of fault healing during the earthquake cycle. Nature 391(6662):69–72

Martin III, Randolph J (1980) Pore pressure stabilization of failure in Westerly granite. Geophys Res Lett 7(5):404–406

Ougier-Simonin A, Zhu W (2015) Effect of pore pressure buildup on slowness of rupture propagation. J Geophys Res: Solid Earth 120(12):7966–7985

Rice JR (1975) On the stability of dilatant hardening for saturated rock masses. J Geophys Res 80(11):1531–1536

Rudnicki JW, Chen C-H (1988) Stabilization of rapid frictional slip on a weakening fault by dilatant hardening. J Geophys Res: Solid Earth 93(B5):4745–4757

Samuelson J, Elsworth D, Marone C (2009) Shear-induced dilatancy of fluid-saturated faults: experiment and theory. J Geophys Res: Solid Earth. https://doi.org/10.1029/2008JB006273

Sawai M et al (2016) Nucleation of frictional instability caused by fluid pressurization in subducted blueschist. Geophys Res Lett 43(6):2543–2551

Scuderi MM, Collettini C, Marone C (2017) Frictional stability and earthquake triggering during fluid pressure stimulation of an experimental fault. Earth Planet Sci Lett 477:84–96

Sibson RH (1973) Interactions between temperature and pore-fluid pressure during earthquake faulting and a mechanism for partial or total stress relief. Nat Phys Sci 243(126):66–68

Wang W, Scholz CH (1994) Wear processes during frictional sliding of rock: a theoretical and experimental study. J Geophys Res: Solid Earth 99(B4):6789–6799

White M et al (2018) A suite of benchmark and challenge problems for enhanced geothermal systems. Geomech Geophys Geo-Energy Geo-Resour 4(1):79–117

Witherspoon PA et al (1980) Validity of cubic law for fluid flow in a deformable rock fracture. Water Resour Res 16(6):1016–1024

Xing T et al (2019) Stabilizing effect of high pore fluid pressure on slip behaviors of gouge-bearing faults. J Geophys Res: Solid Earth 124(9):9526–9545

Yasuhara H, Marone C, Elsworth D (2005) Fault zone restrengthening and frictional healing: the role of pressure solution. J Geophys Res: Solid Earth. https://doi.org/10.1029/2004JB003327

Ye Z, Vachaparampil A, Zhou X, Ghassemi A, Kneafsey T (2019) February. Failure behavior of the Poorman schist and its fractures from EGS collab stimulation site. In 44th workshop on geothermal reservoir engineering

Yoon CE et al (2017) Seismicity during the initial stages of the Guy-Greenbrier, Arkansas, earthquake sequence. J Geophys Res: Solid Earth 122(11):9253–9274

Zhang S, Tullis TE, Scruggs VJ (1999) Permeability anisotropy and pressure dependency of permeability in experimentally sheared gouge materials. J Struct Geol 21(7):795–806